Flexural strike-slip basins

Derek Neuharth[1,2], Sascha Brune[1,2], Anne Glerum[1], Chris K. Morley[3], Xiaoping Yuan[1,4], Jean Braun[1,2]

[1]*GFZ German Research Centre for Geosciences, Telegrafenberg, 14473 Potsdam, Germany.*

[2]*Institute of Geosciences, University of Potsdam, Germany.*

[3]*PTTEP, Enco, Vibhavadi-Rangsit Road, Chatuchak, Bangkok, 10900, Thailand*

[4]*School of Earth Sciences, China University of Geosciences, Wuhan, China*

ABSTRACT

Strike-slip faults are classically associated with pull-apart basins where continental crust is thinned between two laterally offset fault segments. Here we propose a subsidence mechanism to explain the formation of a new type of basin where no substantial segment offset or syn-strike-slip thinning is observed. Such "flexural strike-slip basins" form due to a sediment load creating accommodation space by bending the lithosphere. We use a two-way coupling between the geodynamic code ASPECT and surface processes code FastScape to show that flexural strike-slip basins emerge if sediment is deposited on thin lithosphere close to a strike-slip fault. These conditions were met at the Andaman Basin Central Fault, where seismic reflection data provide evidence of a laterally extensive flexural basin with a depocenter located parallel to the strike-slip fault trace.

MOTIVATION

Near plate boundaries, sedimentary basins usually form by filling accommodation space created via two tectonic processes (Allen & Allen, 2013): 1) isostatic subsidence due to lithospheric stretching or cooling, which particularly governs rift basin formation at divergent boundaries and 2) lithospheric flexure, which is closely associated with foreland basins in convergent settings. So far, basins at transform plate boundaries are thought to be related to the first process, by generating pull-apart basins.

Pull-apart basins form between laterally offset strike-slip fault segments (Mann et al., 1983). During strike-slip motion, the area between the offset faults is extended and rapid basement subsidence is generated due to abrupt crustal thinning (van Wijk et al., 2017). Pull-apart basins lengthen over time, but as they are confined within the overstep, they form as long thin basins with a depocenter that is bounded by the strike- or oblique-slip segments (Seeber et al., 2004). While there are many pull-apart basin examples (e.g., Dead Sea Basin, Garfunkel & Ben-Avraham, 1996; Death Valley Basin, SERPA et al., 1988), there has not been much discussion on other types of strike-slip basins.

Flexural basins form when an overlying load deflects the lithosphere. This is the case during mountain building, wherein the orogenic load creates accommodation space for sediment infill, increasing sedimentation. However under certain conditions basement subsidence may be a consequence, and not a cause, of enhanced sedimentation (Morley & Westaway, 2006). Previously, the process of sedimentation-induced lower crustal flow and accommodation space creation has been suggested where deep sedimentary basins form in areas featuring very weak lower crust (Clift et al., 2015), such as in the fans of the Red (Clift and Sun, 2006) and Pearl Rivers (Dong et al., 2020), both located at the northern continental margin of the South China Sea.

Generalizing conditions for sedimentation-induced creation of accommodation space, we infer that it requires 1) an easily deformable tectonic environment, and 2) focused sedimentation, both of which can occur in regions of prior tectonic subsidence. Considering that strike-slip faults have been suggested to represent highly weakened plate boundaries (Zoback et al., 1987; Provost and Houston, 2003), and that transform continental margins often follow a phase of thinning (Jourdon et al., 2021), we formulate the key hypothesis of this study: sedimentary loading near strike-slip faults in subsided regions may further generate basement subsidence and accommodation space. This positive feedback between focused sedimentation and isostatic flexural subsidence leads to the creation of a previously unrecognized type of basin that we term "flexural strike-slip basin". We test our hypothesis by two means: 1) numerical forward modeling of a strike-slip system subjected to asymmetric sedimentation, and 2) interpreting seismic reflection data from the East Andaman Basin in the Andaman Sea.

GEOLOGICAL SETTING OF THE ANDAMAN SEA

During the Cenozoic, the Andaman sea formed as a transtensional backarc basin due to the coupling of India to western Myanmar (Curray, 2005). Multiple strike-slip faults exist in the region, one being the Sagaing Fault (SF, Fig. 1), an active (18 mm/yr, Maurin et al., 2010; Vigny et al., 2003) fault in the north of the region that connects south-westward to the Andaman spreading center (Curray, 2005). However, south of the SF is another, inactive, strike-slip fault: the Andaman Basin Central Fault (ABCF; Morley, 2016, 2017; Mahattanachai et al., 2021).

The Andaman Sea's transtensional motion led to subsidence, causing the area to act as a sediment trap. Fault trends suggest the region near the ABCF experienced ENE-WSW extension in the Oligocene that shifted to NNW-SSE strike-slip motion during the early to mid-Miocene (lasting ~5 Myr; Morley, 2017). The ABCF formed in a previous necking zone of hyperextended

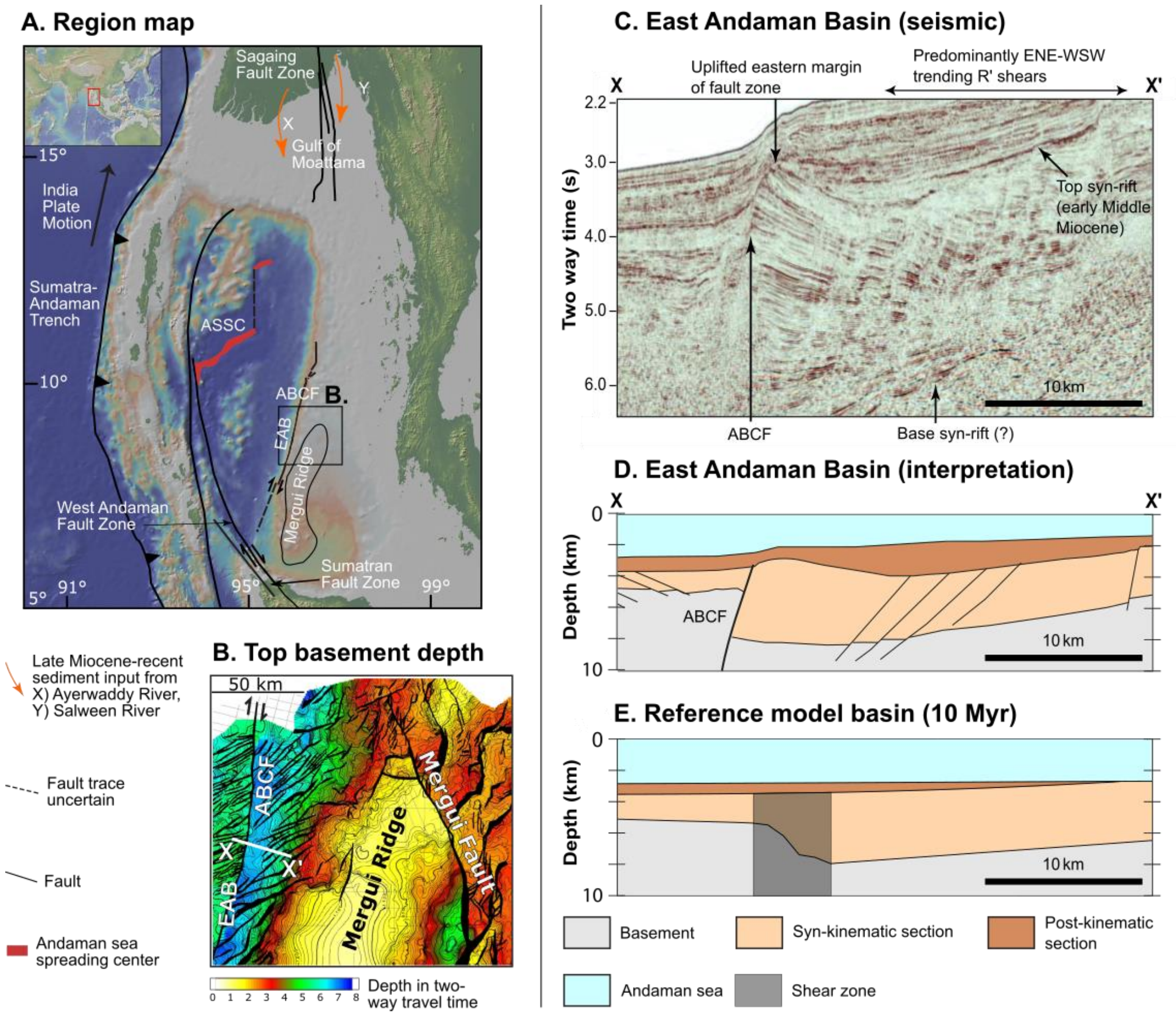

Figure 1. **A. Andaman Sea Map. ASSC: Andaman Sea Spreading Center. ABCF: Andaman Basin Central Fault. EAB: East Andaman Basin. B. Depth to the top basement in two-way travel time. C. Seismic data of the EAB. D. Depth interpretation of C. E. Modeled basin. Post-kinematic sediment is found by applying the additional basement subsidence from 5 to 10 Myr to the topography at 5 Myr.**

continental crust (7-10 km thick; Morley, 2017; Mahattanachai et al., 2021), likely because mantle heterogeneities influence fault location (Phillips et al., 2021). During strike-slip motion, the easterly Mergui Ridge (MR) was partially subaerial and acted as an asymmetric clastic sediment source for the East Andaman Basin (EAB) located along the ABCF (Mahattanachai et al., 2021).

The geometry of the EAB in relation to the ABCF is described in detail by Mahattanachai et al. (2021), who concluded that the long (>200 km), deep (>4 km), westward-thickening basin on the east side of the sub-vertical ABCF did not fit classic extensional, or pull-apart basin characteristics.

MODEL SETUP AND EVOLUTION

We reproduce the key aspects of the EAB region, namely that of thin lithosphere and asymmetric sedimentation, using a visco-plastic 100×8×120 km (X, Y, Z) 3D box model via a two-way coupling of the tectonic code ASPECT (Fig. 1B,C; Kronbichler et al., 2012; Heister et al., 2017; Glerum et al., 2018; Bangerth et al., 2019; supplementary text S1) and the surface processes code FastScape (Braun & Willett, 2013; Yuan et al., 2019a, 2019b; text S2). We assume that a previous extensional event left the region submarine with thinned 40 km thick lithosphere. The model is initialized with 4 km upper crust, 4 km lower crust, 32 km mantle lithosphere, and 80 km of asthenosphere (Fig. 1B; Fig. S1). In Fig. 1B, the east boundary is no-slip in all directions, the west boundary is no-slip in the Z direction, 20 mm/yr in Y to induce strike-slip motion, and is given a small (0.2 mm/yr) extensional component in X which helps avoid bending-induced compression but does not affect the presented results (Fig. S2) . The north and south boundaries are periodic to simulate an infinitely long strike-slip fault, and the initial lithostatic pressure at a reference location is prescribed on the bottom boundary to allow for outflow in response to sedimentation. The strike-slip fault forms self-consistently above an initial perturbation of the Lithosphere-Asthenosphere Boundary (10% of lithosphere thickness) in the center of the model that acts as a weak zone for deformation to localize. Accumulated plastic strain weakens the angle of friction over an interval of 0 to 1 from an initial value of 30° to a final value of 7.5°, promoting brittle localization.

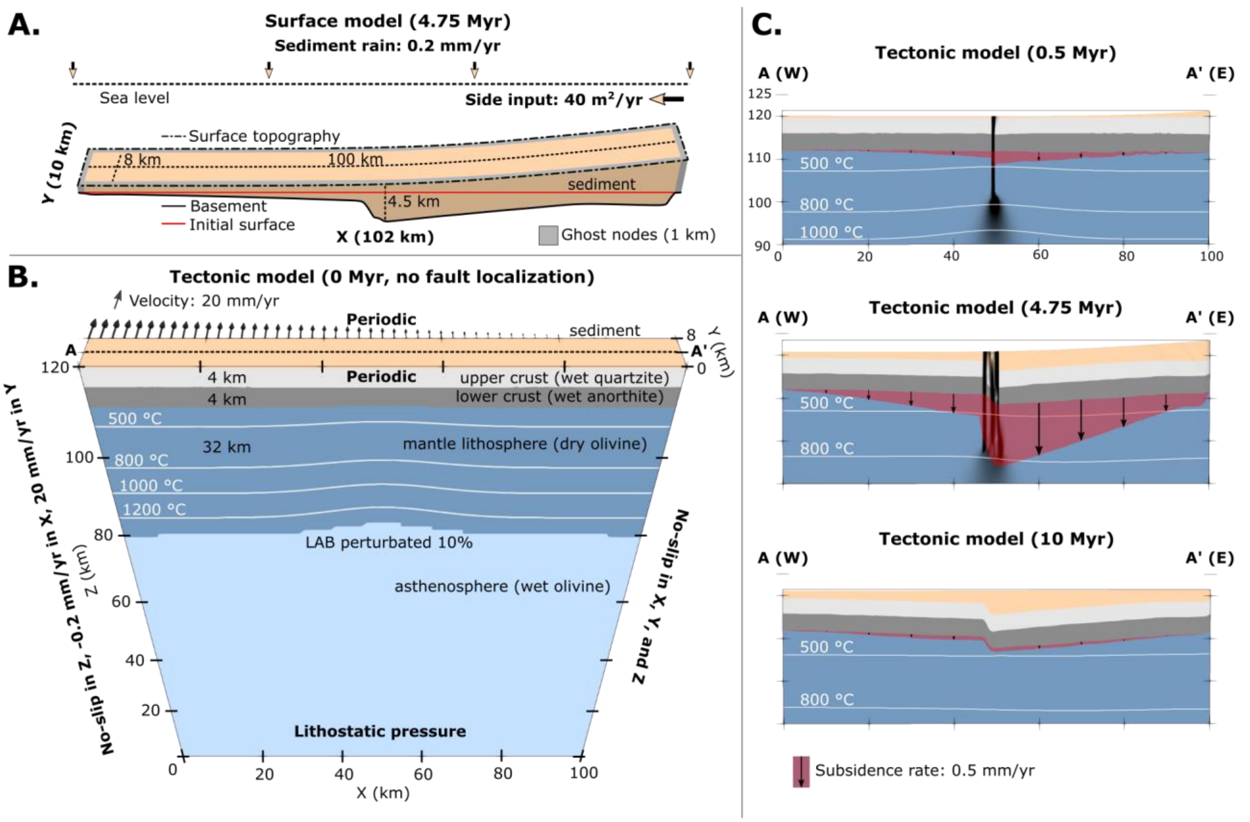

Figure 2. A. Surface processes model at 4.75 Myr and 2× vertical exaggeration. Sediment is the area between the topography (dashed line) and basement (solid black line). Ghost nodes (gray), implemented for periodic advection along Y and to control the sedimentary side input, surround the surface model and do not interact with the tectonic model. B. Initial tectonic setup. Colors represent composition, white isotherms the temperature distribution. Arrows indicate the total velocity magnitude. LAB: Lithosphere-Asthenosphere Boundary. C. Cross-sections of the top 30 km of the tectonic model along A to A' in B showcase the formation of a flexural strike-slip basin in response to sedimentation. Subsidence rate at the Moho is indicated in red. See movies S1 and S2.

The surface processes code FastScape is coupled to the top of the tectonic model (text S3). We assume that the model is submarine and transports sediment via diffusion with a coefficient of 500 m^2/yr, consistent with open marine environments in previous modeling studies (Rouby et al., 2013). Sediment is supplied to the domain in two ways: 1) The entire surface experiences 0.2 mm/yr of pelagic/hemipelagic "sediment rain" sedimentation. 2) Ghost nodes (see Fig. 1A) at the east boundary are uplifted each timestep to prescribe a constant sediment flux of 40 m^2/yr, mimicking an off-model sediment source, similar to the MR for the EAB.

The models are run for 10 Myr, where the first 5 Myr represent the syn-tectonic stage with strike-slip motion and sedimentation. The final 5 Myr constitute the post-tectonic stage with no prescribed motion or sediment supply, although marine sediment transport continues (for setup details, see text S4).

REFERENCE MODEL RESULTS

In the reference model, strain localizes on a vertical fault near the model center (~0.5 Myr; Fig. 1C). Both sides of the fault subside due to the influx of sediment, with the eastern side sinking faster (1.0 vs. 0.4 mm/yr at 4.75 Myr). By 5 Myr, the eastern side of the fault has subsided almost 4 times more than the western side (3.6 vs. 1.0 km), rotating the strike-slip fault to a sub-vertical dip. Following the halt of strike-slip motion and sedimentation, the subsidence rate lowers to 0.08 mm/yr as the sediment hill along the eastern boundary is distributed across the surface. By 10 Myr, both sides have subsided another 0.4 km, and each basin is thickest next to the fault and thins strike-perpendicularly.

The model indicates that flexural strike-slip basins emerge due to sedimentation above thin lithosphere close to strike-slip faults. In contrast to classical half-grabens, these basins form without a significant extensional component.

To test controls on flexural strike-slip basin formation, we run a series of models varying in sedimentation rate, lithospheric thickness, and fault strength. We first focus on sedimentation rate by altering the eastern side influx from 0 (i.e. only sediment rain) to 60 m^2/yr (Fig. 2A-D). With no side input, both sides subside evenly forming a synformal basin that is thickest at the fault (Fig. 2A). This suggests that the asymmetry of the reference model basin is primarily affected by the sedimentation, and not the initial perturbation. At higher side input, the eastern side sinks more, from a maximum basement deflection of 0.9 km with no input to 5.7 km for 60 m^2/yr of input (Fig. 2D). The western side also shows greater deflection with higher eastern sediment input although it is not as pronounced (0.8 to 1.6 km), suggesting either that the sides are not fully decoupled or that more sediment reached the western side.

Next, we vary the lithospheric thickness from 60 to 30 km (Fig. 2E-H). The flexural basement deflection reduces for thicker, more rigid, lithosphere, from a maximum eastern

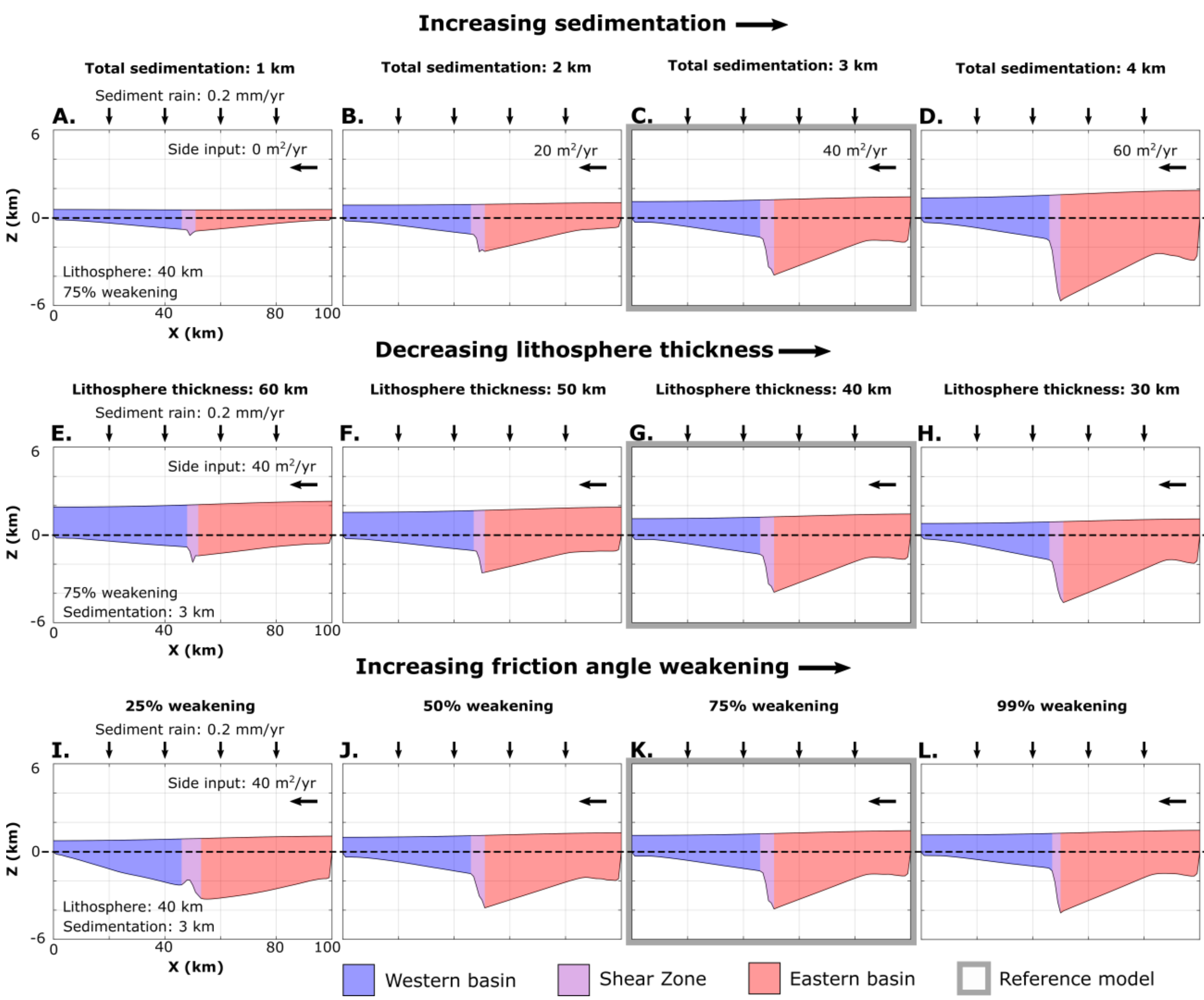

Figure 3. Basin formation when subject to variable sediment input (A-D), lithosphere thickness (E-H), and fault weakening (I-L). Dashed lines along 0 show the initial model elevation. Total sedimentation is the sediment thickness assuming even distribution across the model.

deflection of 4.6 km at 30 km thick lithosphere to 1.4 km at 60 km thick lithosphere. This suggests that it is unlikely for deep flexural basins to form in regions with thick lithosphere.

Finally, we vary the amount of friction angle weakening (Fig. 2I-L). This shows that fault strength affects flexural subsidence (4.2 vs. 3.3 km deflection at 99% and 25% weakening, respectively). At high strength (less weakening), the two lithosphere sides are more coupled and subside together. At low strength, the sides are decoupled and more sensitive to asymmetric sedimentation.

FLEXURAL STRIKE-SLIP BASINS IN THE ANDAMAN SEA

Seismic data suggest the EAB as an asymmetric basin that spans both sides of the ABCF (Mahattanachai et al., 2021). On the western side, basin thickness is relatively uniform (1-2 km; Fig. 3A). Along the fault on the eastern side the basin is substantially thicker (~5 km) and thins to the east towards the sediment source areas of the MR and Peninsular Thailand.

The Gulf of Moattama Basin (GMB) formed along the active SF, and similarly does not fit the pull-apart basin criteria. The GMB basin depocenter is located along the fault, however, unlike the EAB, sediment thicknesses are relatively symmetric across the fault (e.g., Morley & Alvey, 2015). While the EAB received sediment perpendicular to the fault trace, the GMB received sediment axially from the northern Ayerwaddy and Salween rivers (Morley & Alvey, 2015).

We suggest that the primary requirement for flexural strike-slip basin formation is weak or thin lithosphere in an area of high sedimentation. There are two basin types controlled by the sedimentation pattern: 1) when sedimentation is symmetric and both sides receive a similar sediment load (Fig. 2A), a *symmetric basin* forms; 2) for asymmetric sedimentation, two distinct basin sides may form that subside depending on the sediment load they receive (*asymmetric basin*;

Fig. 2C). In both types, the maximum flexure and basin depocenter occur along the fault, and the basin thins strike-perpendicularly.

The Andaman sea provides likely examples for both flexural strike-slip basin types. 1) The GMB, where northern axial sedimentation provided relatively even sedimentation to each side of the fault forming a *symmetric flexural basin*. While this basin would not have experienced purely uniform sedimentation, it shows a similar synformal geometry with the depocenter along the fault as in Fig. 2A. 2) The EAB (Fig. 3), where perpendicular sedimentation from the MR forced greater flexure on the eastern side of the fault. This sedimentation pattern led to an *asymmetric flexural basin*. The EAB and reference model basin both have a change in sediment thickness across the fault, and basin thinning toward the sediment source. Furthermore, basin thicknesses (excluding post-kinematic sediment) along the fault's eastern side (4.5 vs. 4.8 km in the model and EAB, respectively) and western side (1.8 vs. 1.6 km) are comparable.

Despite the similarities, there are some discrepancies between the modeled basin and the EAB. Eastward thinning is less pronounced in the model. As the basement slope is primarily affected by the lithosphere thickness and sediment load, three possible explanations are: 1) The ABCF is capped by a regional unconformity with the post-kinematic sediments (Morley, 2017; Srisuriyon & Morley, 2014), and the fault may have received more sediment while active than expected from the seismic data. 2) The ABCF formed in a necking zone and, as the lithosphere thickness is not well-constrained, it varied spatially and may have been thinner than the 40 km value used here. 3) A more significant syn-strike-slip extensional component would have further deepened the basin along the fault (Sobolev et al., 2005).

Here we focused on the Andaman Sea, but the key requirements for flexural strike-slip basins – thin lithosphere, focused sedimentation, and a weak fault – are possibly met in the New

Guinea Basin in the Bismarck Sea (Fig. S3; Martinez and Taylor, 1996) or the Yinggehai Basin in the South China Sea (Fig. S4; Clift and Sun, 2006), but new seismic data are needed to test this hypothesis. Another candidate is the Gyeongsang Basin in SE Korea, which formed in a transtensional back-arc that shifted into strike-slip motion (Cheon et al., 2020). Smaller-scale flexural strike-slip basins may form within larger pull-apart regions. Examples of these could be the Flat Basin along the East Anatolian Fault (Garcia Moreno et al., 2011) or the Navassa Basin in the Jamaica Passage (Fig. S5; Corbeau et al., 2016), which are faultward dipping strike-slip basins that are not located between offset segments.

CONCLUSION

This study suggests a new class of flexural basins that form along strike-slip faults. These basins are characterized by a fault-parallel depocenter and sediment that thins strike-perpendicularly. The basins can be classified in two types, which are both represented in the Andaman Sea: 1) *symmetric flexural basins*, where axial sedimentation causes a synformal shape, as seen in the GMB, and 2) *asymmetric flexural basins*, where asymmetric sedimentation forces one basin side to subside more than the other, as seen in the EAB.

Flexural strike-slip basins form due to a strike-slip fault that acts as a weak zone facilitating differential subsidence due to sediment loading. The fault decouples the lithosphere sides, allowing them to respond independently to the sediment load they receive. This decoupling makes the sedimentation pattern important for the resulting basin symmetry. For a flexural strike-slip basin to form two criteria must be met: the strike-slip fault must 1) cut through thin lithosphere and 2) be subjected to a sufficient tectonic load.

ACKNOWLEDGMENTS

This study was conducted within the Helmholtz Young Investigators Group CRYSTALS (VH-NG-1132). We thank the Computational Infrastructure for Geodynamics (geodynamics.org), which is funded by the National Science Foundation under award EAR- 0949446 and EAR-1550901, for supporting the development of ASPECT. The work was supported by the North-German Supercomputing Alliance (HLRN). The files and information to replicate these models are found at http://doi.org/10.5281/zenodo.4893421. Figures were made using ParaView, InkScape, and GeoMapApp. We thank PPTEP for providing the 2D seismic data.

REFERENCES

Allen, P.A., and Allen, J.R., 2013, Basin Analysis 3rd edition:, doi:10.1017/CBO9781107415324.004.

Bangerth, W., Dannberg, J., Gassmoeller, R., and Heister, T., 2019, ASPECT v2.1.0: Zenodo, https://doi.org/10.5281/zenodo.2653531.

Braun, J., and Willett, S.D., 2013, A very efficient O(n), implicit and parallel method to solve the stream power equation governing fluvial incision and landscape evolution: Geomorphology, v. 180–181, p. 170–179, doi:10.1016/j.geomorph.2012.10.008.

Cheon, Y., Ha, S., Lee, S., and Son, M., 2020, Tectonic evolution of the Cretaceous Gyeongsang Back-arc Basin, SE Korea: Transition from sinistral transtension to strike-slip kinematics: Gondwana Research, v. 83, p. 16–35, doi:10.1016/j.gr.2020.01.012.

Clift, P.D., Brune, S., and Quinteros, J., 2015, Climate changes control offshore crustal structure at South China Sea continental margin: Earth and Planetary Science Letters, v. 420, p. 66–72, doi:10.1016/j.epsl.2015.03.032.

Clift, P.D., and Sun, Z., 2006, The sedimentary and tectonic evolution of the Yinggehai-Song Hong basin and the southern Hainan margin, South China Sea: Implications for Tibetan uplift and monsoon intensification: Journal of Geophysical Research: Solid Earth, v. 111, p. 1–28, doi:10.1029/2005JB004048.

Corbeau, J., Rolandone, F., Leroy, S., Mercier de Lépinay, B., Meyer, B., Ellouz-Zimmermann, N., and Momplaisir, R., 2016, The northern Caribbean plate boundary in the Jamaica Passage: Structure and seismic stratigraphy: Tectonophysics, v. 675, p. 209–226, doi:10.1016/j.tecto.2016.03.022.

Curray, J.R., 2005, Tectonics and history of the Andaman Sea region: Journal of Asian Earth Sciences, v. 25, p. 187–232, doi:10.1016/j.jseaes.2004.09.001.

Dong, M., Zhang, J., Brune, S., Wu, S., Fang, G., and Yu, L., 2020, Quantifying Postrift Lower Crustal Flow in the Northern Margin of the South China Sea: Journal of Geophysical Research: Solid Earth, v. 125, doi:10.1029/2019JB018910.

Garcia Moreno, D., Hubert-Ferrari, A., Moernaut, J., Fraser, J.G., Boes, X., Van Daele, M., Avsar, U., Çağatay, N., and De Batist, M., 2011, Structure and recent evolution of the Hazar Basin: A strike-slip basin on the East Anatolian Fault, Eastern Turkey: Basin Research, v. 23, p. 191–207, doi:10.1111/j.1365-2117.2010.00476.x.

Garfunkel, Z., and Ben-Avraham, Z., 1996, The structure of the Dead Sea basin: Tectonophysics, v. 266, p. 155–176, doi:10.1016/S0040-1951(96)00188-6.

Glerum, A., Thieulot, C., Fraters, M., Blom, C., and Spakman, W., 2018, Nonlinear viscoplasticity in ASPECT: Benchmarking and applications to subduction: Solid Earth, v. 9, p. 267–294, doi:10.5194/se-9-267-2018.

Heister, T., Dannberg, J., Gassmöller, R., and Bangerth, W., 2017, High Accuracy Mantle Convection Simulation through Modern Numerical Methods – II: Realistic Models and Problems.: Geophysical Journal International, v. 210, p. 833–851, doi:doi:10.1093/gji/ggx195.

Jourdon, A., Kergaravat, C., Duclaux, G., and Huguen, C., 2021, Looking beyond kinematics: 3D thermo-mechanical modelling reveals the dynamics of transform margins: Solid Earth, v. 12, p. 1211–1232, doi:10.5194/se-12-1211-2021.

Kronbichler, M., Heister, T., and Bangerth, W., 2012, High Accuracy Mantle Convection Simulation through Modern Numerical Methods.: Geophysical Journal International, v. 191, doi:doi:10.1111/j.1365-246x.2012.05609.x.

Mahattanachai, T., Morley, C.K., Charusiri, P., and Kanjanapayont, P., 2021, The Andaman Basin Central Fault Zone, Andaman Sea: Characteristics of a major deepwater strike-slip fault system in a polyphase rift: Marine and Petroleum Geology, p. 104997, doi:10.1016/j.marpetgeo.2021.104997.

Mann, P., Hempton, M.R., Dwight, C.B., and Burke, K., 1983, Development of Pull-Apart Basins Authors: Paul Mann , Mark R . Hempton , Dwight C . Bradley and Kevin Burke Published by : The University of Chicago Press Stable URL : http://www.jstor.org/stable/30064017 . All use subject to JSTOR Terms and Conditio: The Journal of Geology, v. 91, p. 529–554.

Martinez, F., and Taylor, B., 1996, Backarc spreading, rifting, and microplate rotation, between transform faults in the Manus Basin: Marine Geophysical Researches, v. 18, p. 203–224, doi:10.1007/BF00286078.

Maurin, T., Masson, F., Rangin, C., Min, U.T., and Collard, P., 2010, First global positioning system results in northern Myanmar: Constant and localized slip rate along the Sagaing fault: Geology, v. 38, p. 591–594, doi:10.1130/G30872.1.

Morley, C.K., 2017, Cenozoic rifting, passive margin development and strike-slip faulting in the Andaman Sea: A discussion of established v. New tectonic models: Geological Society Memoir, v. 47, p. 27–50, doi:10.1144/M47.4.

Morley, C.K., 2016, The impact of multiple extension events, stress rotation and inherited fabrics on normal fault geometries and evolution in the Cenozoic rift basins of Thailand: Geological Society, London, Special Publications, v. 439, p. 413–445, doi:https://doi.org/10.1144/SP439.3.

Morley, C.K., and Alvey, A., 2015, Is spreading prolonged, episodic or incipient in the Andaman Sea? Evidence from deepwater sedimentation: Journal of Asian Earth Sciences, v. 98, p. 446–456, doi:10.1016/j.jseaes.2014.11.033.

Morley, C.K., and Westaway, R., 2006, Subsidence in the super-deep Pattani and Malay basins of Southeast Asia: A coupled model incorporating lower-crustal flow in response to post-rift sediment loading: Basin Research, v. 18, p. 51–84, doi:10.1111/j.1365-2117.2006.00285.x.

Phillips, T.B., Naliboff, J.B., Mccaffrey, K.J.W., Pan, S., and van Hunen, J., 2021, The influence of crustal strength on rift geometry and development - Insights from 3D numerical modelling: [preprint], doi:https://doi.org/10.31223/X58K61.

Provost, A.-S., and Houston, H., 2003, Stress orientations in northern and central California: Evidence for the evolution of frictional strength along the San Andreas plate boundary system: Journal of Geophysical Research: Solid Earth, v. 108, p. 1–18, doi:10.1029/2001jb001123.

Rouby, D., Braun, J., Robin, C., Dauteuil, O., and Deschamps, F., 2013, Long-term stratigraphic evolution of Atlantic-type passive margins: A numerical approach of interactions between surface processes, flexural isostasy and 3D thermal subsidence: Tectonophysics, v. 604, p. 83–103, doi:10.1016/j.tecto.2013.02.003.

Seeber, L., Emre, O., Cormier, M.H., Sorlien, C.C., McHugh, C.M.G., Polonia, A., Ozer, N., and Cagatay, N., 2004, Uplift and subsidence from oblique slip: The Ganos-Marmara bend of the North Anatolian Transform, Western Turkey: Tectonophysics, v. 391, p. 239–258, doi:10.1016/j.tecto.2004.07.015.

SERPA, L., DE VOOGD, B., WRIGHT, L., WILLEMIN, J., OLIVER, J., HAUSER, E., and TROXEL, B., 1988, Structure of the central Death Valley pull-apart basin and vicinity from COCORP profiles in the southern Great Basin: GSA Bulletin, v. 100, p. 1437–1450, doi:10.1130/0016-7606(1988)100<1437:SOTCDV>2.3.CO;2.

Sobolev, S. V., Petrunin, A., Garfunkel, Z., and Babeyko, A.Y., 2005, Thermo-mechanical model of the Dead Sea Transform: Earth and Planetary Science Letters, v. 238, p. 78–95, doi:10.1016/j.epsl.2005.06.058.

Srisuriyon, K., and Morley, C.K., 2014, Pull-apart development at overlapping fault tips: Oblique rifting of a Cenozoic continental margin, northern Mergui Basin, Andaman Sea: Geosphere, v. 10, p. 80–106, doi:10.1130/GES00926.1.

Vigny, C., Socquet, A., Rangin, C., Chamot-Rooke, N., Pubellier, M., Bouin, M.-N., Bertrand, G., and Becker, M., 2003, Present-day crustal deformation around Sagaing fault, Myanmar: Journal of Geophysical Research: Solid Earth, v. 108, doi:https://doi.org/10.1029/2002JB001999.

van Wijk, J., Axen, G., and Abera, R., 2017, Initiation, evolution and extinction of pull-apart basins: Implications for opening of the Gulf of California: Tectonophysics, v. 719–720, p. 37–50, doi:10.1016/j.tecto.2017.04.019.

Yuan, X.P., Braun, J., Guerit, L., Rouby, D., and Cordonnier, G., 2019a, A New Efficient Method to Solve the Stream Power Law Model Taking Into Account Sediment Deposition: Journal of Geophysical Research: Earth Surface, v. 124, p. 1346–1365, doi:10.1029/2018JF004867.

Yuan, X.P., Braun, J., Guerit, L., Simon, B., Bovy, B., Rouby, D., Robin, C., and Jiao, R., 2019b, Linking continental erosion to marine sediment transport and deposition: A new implicit and O(N) method for inverse analysis: Earth and Planetary Science Letters, v. 524, p. 115728, doi:10.1016/j.epsl.2019.115728.

Zoback, M.D. et al., 1987, New evidence on the state of stress of the san andreas fault system: Science, v. 238, p. 1105–1111, doi:10.1126/science.238.4830.1105.

Supplementary Information

Flexural strike-slip basins

Derek Neuharth[1,2], Sascha Brune[1,2], Anne Glerum[1], Chris K. Morley[3], Xiaoping Yuan[1,4], Jean Braun[1,2]

[1]GFZ German Research Centre for Geosciences, Telegrafenberg, 14473 Potsdam, Germany.

[2]Institute of Geosciences, University of Potsdam, Germany.

[3]PTTEP, Enco, Vibhavadi-Rangsit Road, Chatuchak, Bangkok, 10900, Thailand

[4]School of Earth Sciences, China University of Geosciences, Wuhan, China

Contents of this file

Additional supporting information (uploaded separately)

Text S1: ASPECT Methods

1.1 Governing equations

We perform numerical simulations of a 3D strike-slip system using the open source finite-element code ASPECT (Advanced Solver for Problems in Earth's ConvecTion, version 2.3.0-pre; Heister et al., 2017; Kronbichler et al., 2012; Rose et al., 2017; Bangerth et al., 2019). ASPECT solves the following incompressible conservation equations assuming an infinite Prandtl number (i.e. without the inertial term),

$$-\nabla \cdot (2\eta\dot{\varepsilon}) + \nabla P = \rho \mathbf{g} \,, \tag{1}$$

$$\nabla \cdot (\mathbf{u}) = 0 \,, \tag{2}$$

$$\bar{\rho} C_p \left(\frac{\partial T}{\partial t} + \mathbf{u} \cdot \nabla T\right) - \nabla \cdot k \nabla T = \bar{\rho} H + \alpha T (\mathbf{u} \cdot \nabla P) \,, \tag{3}$$

$$\frac{\partial c_i}{\partial t} + \mathbf{u} \cdot \nabla c_i = q_i \,, \tag{4}$$

where equation (1) represents the conservation of momentum, with η the effective viscosity, $\dot{\varepsilon}$ the deviator of the strain rate tensor (defined as $\frac{1}{2}(\nabla \mathbf{u} + (\nabla \mathbf{u})^T)$), $\mathbf{u}$ the velocity, P the pressure, ρ the density, and $\mathbf{g}$ gravity. Equation (2) describes the conservation of volume. Equation (3) represents the conservation of energy where $\bar{\rho}$ is the reference adiabatic density, C_p the specific heat capacity, T the temperature, k the thermal conductivity, H the radiogenic heating, and α the thermal expansivity. As right-hand-side heating terms, we include radioactive heating and adiabatic heating from top to bottom, respectively. Finally, we solve the advection equation (4) for each compositional field c_i (e.g., upper crust, lower crust, and accumulated plastic strain) with reaction rate q_i nonzero only for the plastic strain field.

1.2 Rheology

We use a visco-plastic rheology (Glerum et al., 2018), which additionally includes plastic weakening based on accumulated plastic strain. In the viscous regime, we use a composite of diffusion and dislocation creep (Karato and Wu, 1993), formulated as:

$$\eta_{\mathrm{eff}}^{\mathrm{diff|dis}} = \frac{1}{2} A_{\mathrm{diff|dis}}^{\frac{-1}{n}} d^{m} \dot{\varepsilon}_{e}^{\frac{1-n}{n}} \exp\left(\frac{(E_{\mathrm{diff|dis}} + PV_{\mathrm{diff|dis}})}{nRT}\right), \tag{5}$$

where A is a scalar prefactor, d the grain size, $\dot{\varepsilon}_e$ the square root of second invariant of the deviatoric strain rate, E the activation energy, P the pressure, V the activation volume, R the gas constant, T the temperature, and n the stress exponent. For diffusion, n = 1 and the equation becomes independent of strain rate. For dislocation creep, the grain size exponent m vanishes, rendering dislocation creep independent of grain size. Values for A, E, V, and n used in our models are composition-dependent and found in supplementary Table S1.

In the plastic regime, when viscous stresses exceed the yield stress, we use the Drucker-Prager yield criterion (Davis and Selvadurai, 2002). The effective plastic viscosity is given by

$$\eta_{\mathrm{eff}}^{\mathrm{pl}} = \frac{\frac{6C\cos\phi}{\sqrt{3}(3-\sin\phi)} + \frac{6P\sin\phi}{\sqrt{3}(3-\sin\phi)}}{2\dot{\varepsilon}_e}, \tag{6}$$

where C is the cohesion and ϕ the internal angle of friction. The accumulation of plastic strain is tracked as a compositional field. This field is used to linearly weaken ϕ from an initial value of 30° to a final value of 7.5° over the accumulated plastic strain interval of 0 to 1. The time-integrated value of the strain reaction rate q_i is approximated as $\dot{\varepsilon}_e \cdot dt$ when plastic yielding occurs (with dt the current timestep size).

Text S2: FastScape Methods

FastScape is a landscape evolution code that changes the topographic surface through uplift, advection, the stream-power law (SPL), and hillslope diffusion (Braun and Willett, 2013). It can additionally deposit fluvial sediment (Yuan et al., 2019a) and include a marine component that handles marine sediment (sand/silt) transport and deposition, and layer compaction based on sand/slit porosity (Yuan et al., 2019b). For simplicity, we here assume that the entire model surface is submarine, with uniform properties (i.e., sand and silt transport coefficients are the same), and that there is no compaction (porosity is zero). Hence, FastScape deforms the surface through the uplift rate and marine diffusion equation only as

$$\frac{\mathrm{dh}}{\mathrm{dt}} = \mathbf{U} + \mathrm{K_m}\nabla^2\mathrm{h}\,, \tag{7}$$

where h is the topographic elevation, $\mathbf{U}$ the uplift rate and $\mathrm{K_m}$ the marine diffusion coefficient.

Text S3: ASPECT/FastScape coupling

In this paper we use a two-way coupling of the tectonic ASPECT code and the landscape evolution FastScape code. For this coupling a FastScape shared library is called by an ASPECT plugin to deform its surface. The plugin has 3 main components: 1) Copy the height and velocity values from ASPECT. 2) Initialize and run FastScape. If it is the first timestep of the tectonic model, FastScape will be initialized using height and velocity values from ASPECT. In subsequent timesteps, as FastScape runs separately, it can be at a higher resolution than ASPECT, only the velocity values from ASPECT are transferred to FastScape. Before running FastScape, the initial topography values are saved. After running FastScape, the new and initial topography are compared to determine a nodal Z velocity,

$$\mathbf{V_z} = \frac{h_f - h_i}{dt_a}, \tag{8}$$

where h_i is the initial surface, h_f the final surface, and dt_a the ASPECT timestep. 3) Use the Z velocity field to determine the displacement of the ASPECT mesh surface and interior. This displacement is then interpolated onto the ASPECT surface using the overarching mesh deformation plugin.

The FastScape mesh includes an additional element-size layer of ghost nodes compared to the ASPECT surface mesh. The values in these nodes are not considered when interpolating the surface back to ASPECT and are used primarily to avoid FastScape boundary artifacts being sent to the ASPECT model (e.g., the boundaries do not uplift from advected topography). To avoid possible erroneous sediment flux out or into the model from artificial slopes, each timestep the ghost nodes are updated with the topography and velocity values of the nearest inward node (ASPECT boundary node).

Besides passing ASPECT's uplift velocities, we use the plugin's FastScape interface to supply additional input to the surface process model in two ways: 1) to add marine background sedimentation via the sediment rain effect, and 2) to add a boundary sediment flux using the ghost nodes. For the sediment rain, at each nodal point we update FastScape with a flat height increase every ASPECT timestep equivalent to a rate of 0.2 mm/yr. Second, through the diffusion component in equation (7) we prescribe a constant sediment flux at the boundary assuming that,

$$\mathbf{Q} = K_m S, \tag{9}$$

where **Q** is the sediment flux and S the slope. Since K_m and Q are user-set parameters, to achieve this we alter S by uplifting the boundary ghost nodes every ASPECT timestep so that **Q** remains constant.

Text S4: Model setup

In this study we examine how a strike-slip fault responds to sedimentation. We therefore set up a 3D box model with dimensions 100×8×120 km (X, Y, and Z, where Z is depth) and 5 compositions representing a wet quartzite upper crust (Rutter and Brodie, 2004), wet anorthite lower crust (Rybacki et al., 2006), dry olivine lithospheric mantle, wet olivine asthenosphere (Hirth & Kohlstedt, 2003), and a sediment layer that has rheologic parameters identical to wet quartzite, but with density and temperature parameters consistent with sediment (Sippel et al., 2017). The total crustal thickness is set to 8 km (4 km upper crust, 4 km lower crust) based on crustal estimates of the area (7-10 km; Mahattanachai et al., 2021). The lithospheric mantle extends between the Moho and the lithosphere-asthenosphere boundary (LAB) at 40 km depth. The LAB depth, like the crust, has been perturbed by a previous extensional period. The remaining material beneath the LAB is considered asthenosphere (Fig. S1). While there is no initial sediment layer, the top boundary is fixed to a sediment composition so that any top-inflow of material due to topography changes other than uplift is sediment.

The ASPECT model mesh consists of two element sizes: 1 km and 2 km. The upper 8 km of the model is refined at 1 km to best resolve the crust and forming sediment layer. This high-resolution area is additionally extended to a depth of 35 km from X = 42 km to X = 52 km to better resolve the strike-slip fault. All other areas are refined at 2 km.

The initial temperature above the LAB is determined by a steady-state geotherm (Turcotte and Schubert, 2002), and below by a mantle adiabat. For simplicity, an initial weak zone is seeded through a small perturbation: we raise the LAB locally by 10% of the lithospheric mantle thickness. We fix the top boundary temperature at 0 °C, and the bottom boundary at the temperature initially determined from the mantle adiabat. All other boundaries are set to zero heat-flux.

The coupled model is run for 10 Myr, where the model in the first 5 Myr includes non-zero velocity boundary conditions. During this time, the western boundary is given a strike-slip component of 20 mm/yr (in Y), and an extensional component of 0.2 mm/yr (in X), while Z is set to no-slip. This gives a total of 100 km of dextral strike-slip motion and 1 km of extension. The small extensional component is introduced to avoid compressional pop-ups that form at the shear zone as the lithosphere subsides due to the sediment load (Fig. S2). The exact extensional value is chosen to accommodate horizontal stress forces related to isostatic compensation. From 5-10 Myr, extension and strike-slip motion stop as the western boundary is set to no-slip in all directions. All other boundary conditions are constant for the entire model run, with the eastern boundary being no-slip in all directions, the north and south boundaries set to periodic to simulate an infinitely long strike-slip fault the initial lithostatic pressure computed at a reference location prescribed on the bottom boundary to allow for outflow in response to sedimentation, and the top deformed through the use of FastScape.

FastScape is set up with an arbitrarily high sea level so that the entire model is considered submarine. This setup leads to a model with no acting stream power law, and sediment being moved solely through marine sediment diffusion. For simplicity, we additionally assume that there is no compaction and no difference between sand and silt. As such, we use a diffusion coefficient of 500 m^2/y for both, a value consistent with open marine environments in previous modelling studies (e.g., Rouby et al., 2013). During the syn-strike-slip phase of the tectonic model (0-5 Myr) we supply sediment to the model in two ways: 1) To account for pelagic/hemipelagic sedimentation (sediment rain) we deposit at a constant sedimentation rate of 0.2 mm/yr. 2) We assume there is an asymmetric off-model source of sediment, similar to the eastern Mergui Ridge for the East Andaman Basin, that inputs sediment into the system from the eastern boundary at a rate of 40 m^2/yr. This is done utilizing equation (9), wherein we uplift the ghost nodes at each timestep so that a constant flux is prescribed through marine diffusion. After this syn-tectonic stage, sediment supply to the system is halted, although marine diffusion continues to work on the topography.

Parameter	Symbol	Units	Sediment	Upper crust	Lower crust	Lithospheric mantle	Asthenosphere
Reference density (surface)	ρ_0	kg m^{-3}	2520	2700	2850	3280	3300
Thermal expansivity	α	K^{-1}	$3.7 \cdot 10^{-5}$	$2.7 \cdot 10^{-5}$	$2.7 \cdot 10^{-5}$	$3.0 \cdot 10^{-5}$	$3.0 \cdot 10^{-5}$
Thermal diffusivity	κ	m^2 s^{-1}	$7.28 \cdot 10^{-7}$	$9.26 \cdot 10^{-7}$	$5.85 \cdot 10^{-7}$	$8.38 \cdot 10^{-7}$	$8.33 \cdot 10^{-7}$
Heat capacity	C_p	J kg^{-1} K^{-1}	1200	1200	1200	1200	1200
Heat production	H	W m^{-3}	$1.2 \cdot 10^{-6}$	$1.5 \cdot 10^{-6}$	$0.2 \cdot 10^{-6}$	0	0
Cohesion	C	Pa	$20 \cdot 10^{6}$	$20 \cdot 10^{6}$	$20 \cdot 10^{6}$	$20 \cdot 10^{6}$	$20 \cdot 10^{6}$
Internal friction angle (unweakened)	ϕ	°	30	30	30	30	30
Strain weakening interval	-	-	[0,1]	[0,1]	[0,1]	[0,1]	[0,1]
Strain weakening factor	ϕ_{wf}	-	0.25	0.25	0.25	0.25	0.25
Creep properties			Sediment	Wet quartzite	Wet anorthite	Dry olivine	Wet olivine
Stress exponent (dis)	n	-	4.0	4.0	3.0	3.5	3.5
Constant prefactor (dis)	A_{dis}	Pa^{-n} s^{-1}	$8.57 \cdot 10^{-28}$	$8.57 \cdot 10^{-28}$	$7.13 \cdot 10^{-18}$	$6.52 \cdot 10^{-16}$	$2.12 \cdot 10^{-15}$
Activation energy (dis)	E_{dis}	J mol^{-1}	$223 \cdot 10^{3}$	$223 \cdot 10^{3}$	$345 \cdot 10^{3}$	$530 \cdot 10^{3}$	$480 \cdot 10^{3}$
Activation volume (dis)	V_{dis}	m^3 mol^{-1}	0	0	$38 \cdot 10^{-6}$	$18 \cdot 10^{-6}$	$11 \cdot 10^{-6}$
Constant prefactor (diff)	A_{diff}	Pa^{-1} s^{-1}	$5.79 \cdot 10^{-19}$	$5.79 \cdot 10^{-19}$	$2.99 \cdot 10^{-25}$	$2.25 \cdot 10^{-9}$	$1.5 \cdot 10^{-9}$
Activation energy (diff)	E_{diff}	J mol^{-1}	$223 \cdot 10^{3}$	$223 \cdot 10^{3}$	$159 \cdot 10^{3}$	$375 \cdot 10^{3}$	$335 \cdot 10^{3}$
Activation volume (diff)	V_{diff}	m^3 mol^{-1}	0	0	$38 \cdot 10^{-6}$	$6 \cdot 10^{-6}$	$4 \cdot 10^{-6}$
Grain size (diff)	d	m	0.001	0.001	0.001	0.001	0.001
Grain size exponent (diff)	m	-	2.0	2.0	3.0	0	0

Table S1: ASPECT model parameters.

Parameter	Symbol	Unit	Value
Marine sand transport coefficient	K_{sand}	m^2/yr	500
Surface sand porosity	φ_{sand}	-	0
Sand e-folding depth	z_{sand}	m	0
Marine silt transport coefficient	K_{silt}	m^2/yr	500
Surface silt porosity	φ_{silt}	-	0
Silt e-folding depth	z_{silt}	m	0
Sand-shale ratio	F	-	1
Thickness of transport layer	L	m	100
Sea level	h_{sea}	m	5000

Table S2: FastScape model parameters.

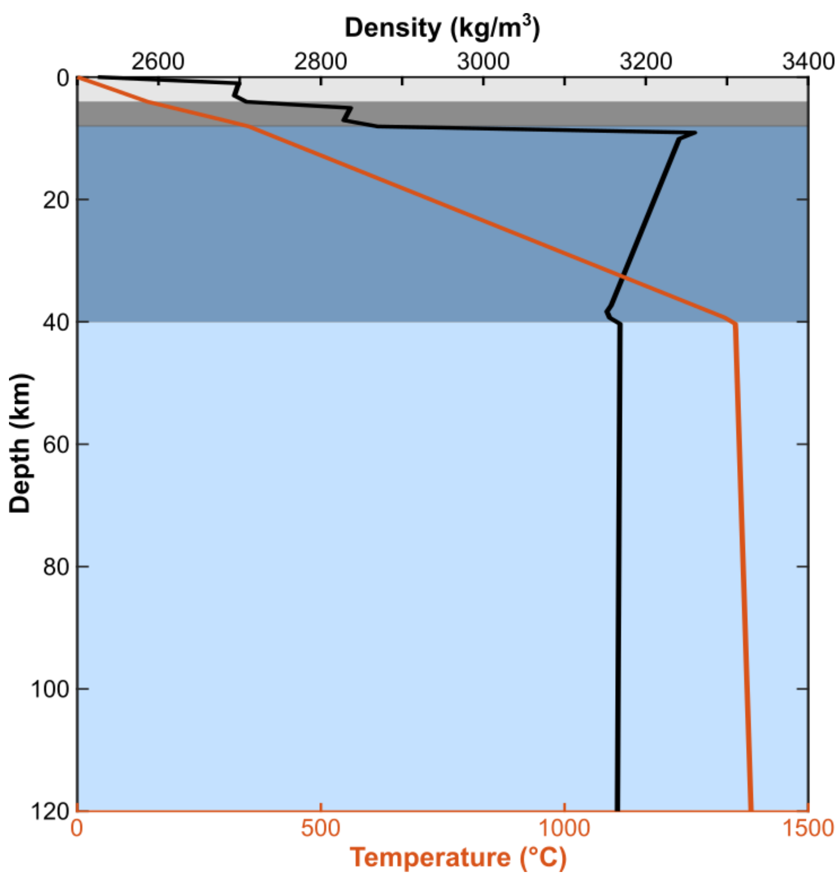

Figure S1: Density (black) and temperature (red) profiles by depth. Colored backgrounds represent the compositions, with light gray (upper crust), dark gray (lower crust), dark blue (mantle lithosphere), and light blue (asthenosphere).

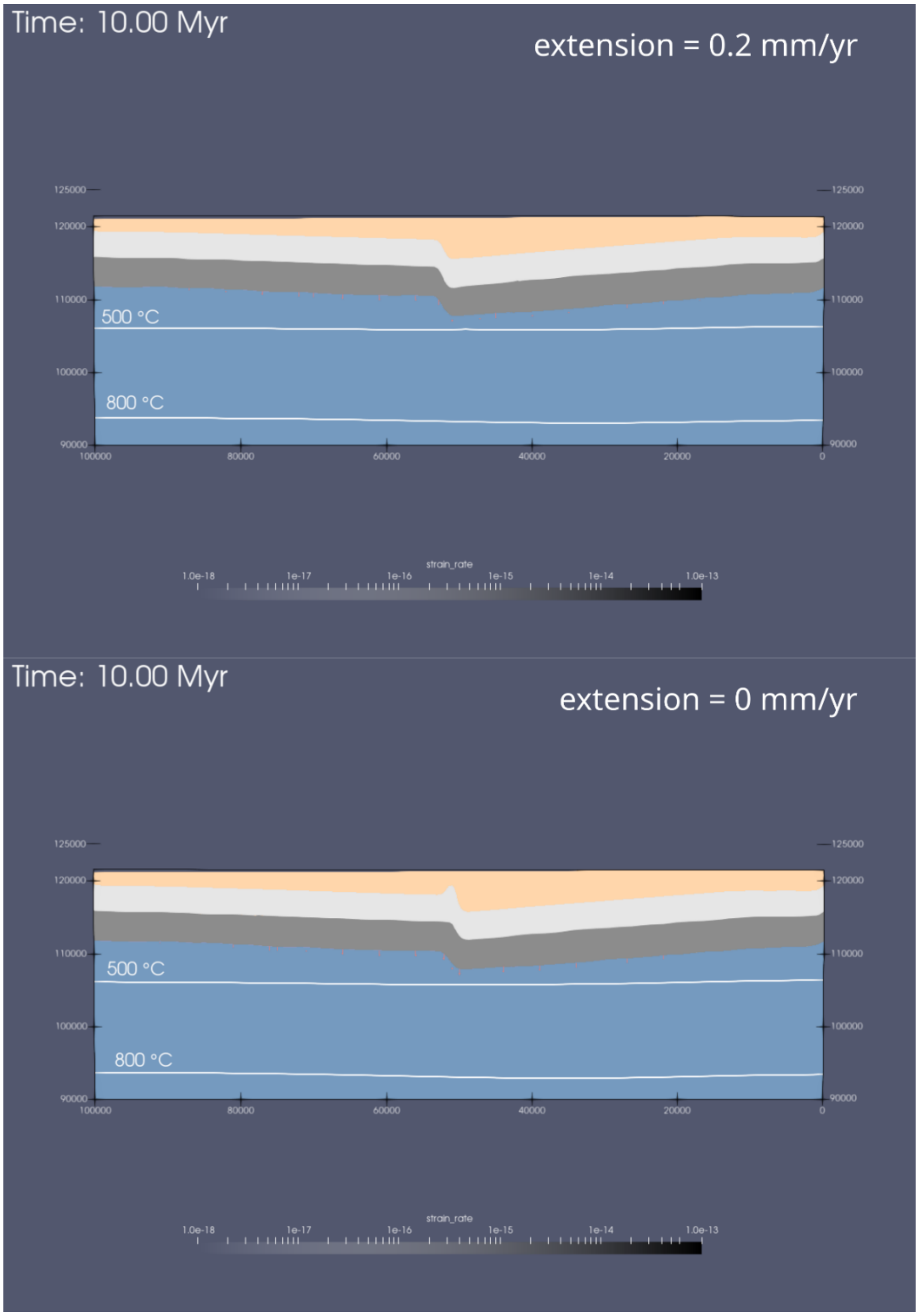

Figure S2: Comparison showing the reference model with A) a 0.2 mm/yr extensional component. B) no extensional component, leading to the formation of a small compressional pop-up in the center.

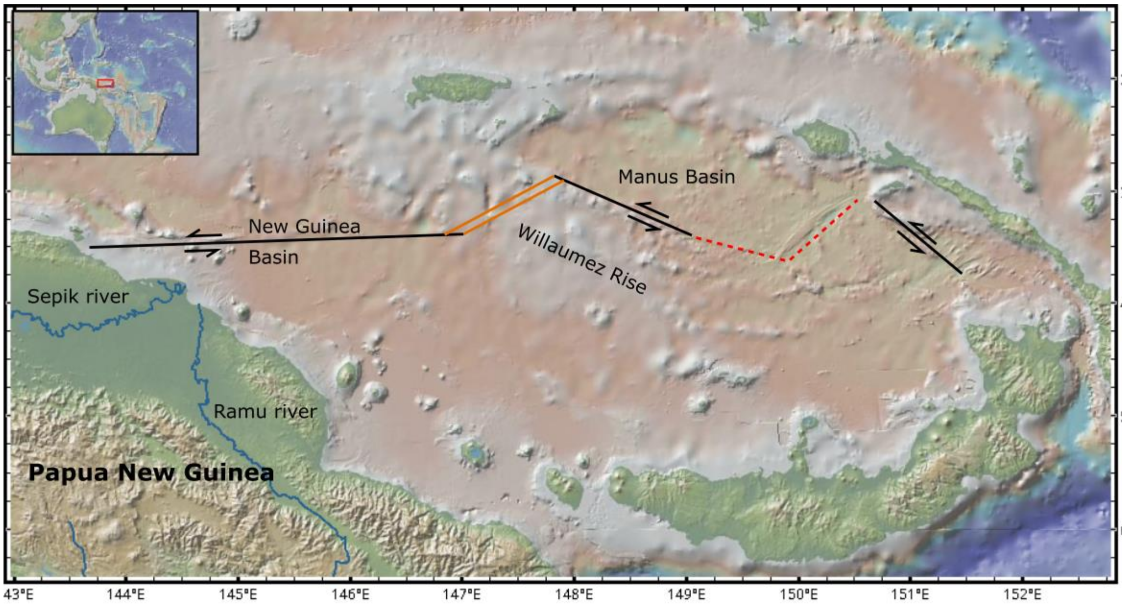

Figure S3: Regional map of the Manus back-arc region, fault locations based on Fig. 1 in Martinez and Taylor, 1996. Black lines indicate strike-slip faults, parallel orange lines spreading centers, dashed red lines lava fields, and blue lines major rivers. This figure was made using GeoMappApp (www.geomapapp.org; Ryan et al., 2009).

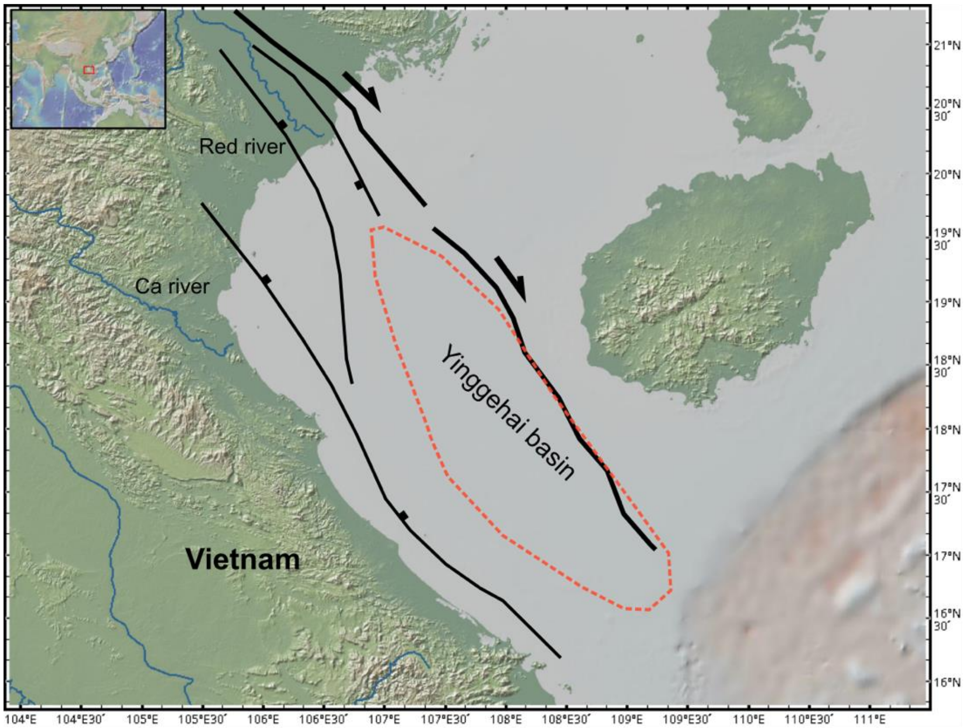

Figure S4: Regional map showing the Red River Fault Zone, and location of the Yinggehai basin. Fault locations based on Fig. 10 in Noda, 2013. Black lines show faults, blue lines major rivers, and the Yinggehai basin is outline in the dashed orange circle. This figure was made using GeoMappApp (www.geomapapp.org; Ryan et al., 2009).

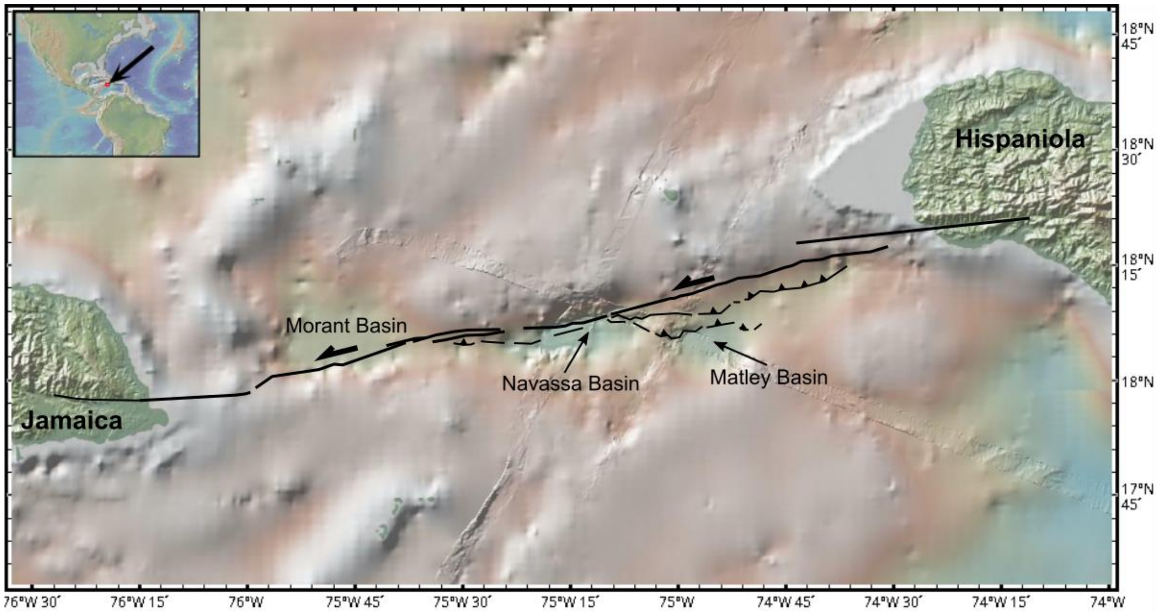

Figure S5: Regional map of the Jamaica Passage showing the Navassa strike-slip basin along the Enriquillo-Plantain-Garden Fault Zone. Fault locations based on Fig. 6 in Corbeau et al., 2016. This figure was made using GeoMappApp (www.geomapapp.org; Ryan et al., 2009).

Video S1: Full evolution of the tectonic reference model (Fig. 2C,K,G). Colors represent composition where tan is sediment, light gray is upper crust, dark gray is lower crust, dark blue is mantle lithosphere, and light blue is the asthenosphere. The white lines are temperature contours, gray-scale the strain rate, and arrows indicate the total velocity magnitude.

Video S2: Evolution of the middle slice of the top 30 km of the reference tectonic model. Colors represent composition where tan is sediment, light gray is upper crust, dark gray is lower crust, dark blue is mantle lithosphere, and light blue is the asthenosphere. The white lines are temperature contours, gray-scale the strain rate, and red arrows indicate the subsidence rate (Z velocity) along the 8 km depth contour.

References

Bangerth, W., Dannberg, J., Gassmoeller, R., and Heister, T., 2019, ASPECT v2.1.0: Zenodo, https://doi.org/10.5281/zenodo.2653531.

Braun, J., and Willett, S.D., 2013, A very efficient O(n), implicit and parallel method to solve the stream power equation governing fluvial incision and landscape evolution: Geomorphology, v. 180–181, p. 170–179, doi:10.1016/j.geomorph.2012.10.008.

Corbeau, J., Rolandone, F., Leroy, S., Mercier de Lépinay, B., Meyer, B., Ellouz-Zimmermann, N., and Momplaisir, R., 2016, The northern Caribbean plate boundary in the Jamaica Passage: Structure and seismic stratigraphy: Tectonophysics, v. 675, p. 209–226, doi:10.1016/j.tecto.2016.03.022.

Davis, R.O., and Selvadurai, A.P.., 2002, Plasticity and Geomechanics: Cambridge University Press.

Glerum, A., Thieulot, C., Fraters, M., Blom, C., and Spakman, W., 2018, Nonlinear viscoplasticity in ASPECT: Benchmarking and applications to subduction: Solid Earth, v. 9, p. 267–294, doi:10.5194/se-9-267-2018.

Heister, T., Dannberg, J., Gassmöller, R., and Bangerth, W., 2017, High Accuracy Mantle Convection Simulation through Modern Numerical Methods – II: Realistic Models and Problems.: Geophysical Journal International, v. 210, p. 833–851, doi:doi:10.1093/gji/ggx195.

Hirth, G., and Kohlstedt, D., 2003, Rheology of the upper mantle and the mantle wedge: a view from the experimentalists: Inside the Subudction Factory Geophysical Monograph (American Geophysical Union), v. 183.

Karato, S., and Wu, P., 1993, Rheology the Upper Mantle : Synthesis: v. 260.

Kronbichler, M., Heister, T., and Bangerth, W., 2012, High Accuracy Mantle Convection Simulation through Modern Numerical Methods.: Geophysical Journal International, v. 191, doi:doi:10.1111/j.1365-246x.2012.05609.x.

Mahattanachai, T., Morley, C.K., Charusiri, P., and Kanjanapayont, P., 2021, The Andaman Basin Central Fault Zone, Andaman Sea: Characteristics of a major deepwater strike-slip fault system in a polyphase rift: Marine and Petroleum Geology, p. 104997, doi:10.1016/j.marpetgeo.2021.104997.

Martinez, F., and Taylor, B., 1996, Backarc spreading, rifting, and microplate rotation, between transform faults in the Manus Basin: Marine Geophysical Researches, v. 18, p. 203–224, doi:10.1007/BF00286078.

Noda, A., 2013, Strike-Slip Basin – Its Configuration and Sedimentary Facies: Mechanism of

Sedimentary Basin Formation - Multidisciplinary Approach on Active Plate Margins, doi:10.5772/56593.

Rose, I., Buffett, B., and Heister, T., 2017, Stability and Accuracy of Free Surface Time Integration in Viscous Flows.: Physics of the Earth and Planetary Interiors, v. 262, p. 90–100, doi:doi:10.1016/j.pepi.2016.11.007.

Rouby, D., Braun, J., Robin, C., Dauteuil, O., and Deschamps, F., 2013, Long-term stratigraphic evolution of Atlantic-type passive margins: A numerical approach of interactions between surface processes, flexural isostasy and 3D thermal subsidence: Tectonophysics, v. 604, p. 83–103, doi:10.1016/j.tecto.2013.02.003.

Rutter, E.H., and Brodie, K.H., 2004, Experimental grain size-sensitive flow of hot-pressed Brazilian quartz aggregates: Journal of Structural Geology, v. 26, p. 2011–2023, doi:10.1016/j.jsg.2004.04.006.

Ryan, W.B.F. et al., 2009, Global Multi-Resolution Topography synthesis: Geochemistry, Geophysics, Geosystems, v. 10, doi:https://doi.org/10.1029/2008GC002332.

Rybacki, E., Gottschalk, M., Wirth, R., and Dresen, G., 2006, Influence of water fugacity and activation volume on the flow properties of fine-grained anorthite aggregates: Journal of Geophysical Research: Solid Earth, v. 111, doi:10.1029/2005JB003663.

Sippel, J., Meeßen, C., Cacace, M., Mechie, J., Fishwick, S., Heine, C., Scheck-Wenderoth, M., and Strecker, M., 2017, The Kenya rift revisited: Insights into lithospheric strength through data-driven 3-D gravity and thermal modelling: Solid Earth, v. 8, p. 45–81, doi:10.5194/se-8-45-2017.

Turcotte, D.L., and Schubert, G., 2002, Geodynamics: Cambridge University Press.

Yuan, X.P., Braun, J., Guerit, L., Rouby, D., and Cordonnier, G., 2019a, A New Efficient Method to Solve the Stream Power Law Model Taking Into Account Sediment Deposition: Journal of Geophysical Research: Earth Surface, v. 124, p. 1346–1365, doi:10.1029/2018JF004867.

Yuan, X.P., Braun, J., Guerit, L., Simon, B., Bovy, B., Rouby, D., Robin, C., and Jiao, R., 2019b, Linking continental erosion to marine sediment transport and deposition: A new implicit and O(N) method for inverse analysis: Earth and Planetary Science Letters, v. 524, p. 115728, doi:10.1016/j.epsl.2019.115728.